Dust emission from crusted surfaces: Insights from field measurements and modelling

Martina Klose[1,2], Thomas E. Gill[3], Vicken Etyemezian[4], George Nikolich[4], Zahra Ghodsi Zadeh[5], Nicholas P. Webb[6], and R. Scott Van Pelt[7]

[1]Barcelona Supercomputing Center (BSC), Barcelona, Spain
[2]previously visiting scientist at USDA-ARS Jornada Experimental Range, Las Cruces, NM, USA
[3]University of Texas at El Paso, Department of Geological Sciences, El Paso, TX, USA
[4]Desert Research Institute, Division of Atmospheric Sciences, Las Vegas, NV, USA
[5]New Mexico State University, Las Cruces, NM, USA
[6]USDA-ARS Jornada Experimental Range, Las Cruces, NM, USA
[7]USDA-ARS Wind Erosion and Water Conservation Research Unit, Big Spring, TX, USA

Correspondence: M. Klose (martina.klose@bsc.es)

Abstract. Crusted surfaces can be major sources of mineral dust emission. Quantitative understanding of dust emission from crusted surfaces is limited, because (1) theories on dust emission are not well tested for such surfaces; and (2) modelling is hampered by a lack of input data sufficient to describe the surface conditions. Combining detailed field measurements with physics-based numerical modelling, we present new insights into dust emission from crusted surfaces. Our measurements confirm that crust erodibility and dust-emission intensity can increase or decrease after previous erosion events. To support interpretation of the measurements and to test the applicability of a state-of-the-art parameterisation to simulate dust emission from crusted surfaces, we apply the dust emission scheme of Shao (2004). Saltation flux, which is input to the scheme, is approximated using the parameterisation of Kawamura (1964) and a scaling factor obtained from observations. Limitations of this approach are discussed. Our results show that the dust emission scheme is suitable to estimate dust emission from crusted surfaces if accurate input data and parameters describing the soil-surface condition are provided. The parameters were optimized for each dust event to achieve a best estimate. The variation of the resulting parameter values confirms the observed variability of dust-emission efficiency between the events and provides further evidence that it was caused by variations in crust erodibility. Our study demonstrates that available physics-based dust-emission parameterisations are able to simulate dust emissions under complicated conditions, but also that refined information on the soil-surface conditions are needed as input to the schemes.

 https://doi.org/10.1016/j.aeolia.2019.05.001

1 Introduction

Mineral dust continues to receive increasing attention in Earth system sciences due to its broad range of impacts on the environment and human daily life (e.g. Middleton, 2017). Understanding of the physics of dust emission along with its impacts remains challenging. An enduring challenge is understanding the effect of the soil surface condition on the mechanisms and amounts of dust emission, in particular when soil conditions are not ideal for dust emission. This can be the case when, for example, on crusted surfaces the supply of loose sand and dust particles readily available for entrainment is limited or heterogeneously distributed (e.g. Raupach and Lu, 2004; Macpherson et al., 2008; Shao, 2008).

Soil crusts, especially those that contain large fractions of clay and silt, are known to effectively reduce the vulnerability of a surface to wind erosion (Gillette et al., 1982; Zobeck, 1991; McKenna Neuman et al., 1996; Rice and McEwan, 2001). However, loose particles and particle aggregates present on top of a crust can still abrade the soil crust, generating dust emission. Zobeck (1991) tested the impact of saltation flux, crust consolidation, and soil chemical and physical properties on abrasion soil loss using laboratory wind tunnel experiments. Zobeck found that abrasion (or saltation bombardment) efficiency was positively correlated with sand content, cation-exchange capacity/clay ratio, and negatively correlated with sand flux and rainfall rate (used to generate the crust). The negative correlation with sand flux is likely due to lower particle velocities in transport-limited compared to particle-supply limited conditions (e.g. Houser and Nickling, 2001b). Rice and McEwan (2001) exposed crusts of varying strength – generated by mixing sand (particle-size range $500 - 1000\,\mu$m) with varying amounts of an erosion-resistant "loamy silt soil" – to bombardment by saltating sand particles ($300 - 355\,\mu$m) in a wind tunnel. Rice and McEwan found that "the saltating particles were able to erode each of the surfaces, although in the case of the strongest crust (...) the erosion rate was small". Generally, the erosion rate decreased with increasing amounts of fine particles, which acted as a cement between the sand grains. Surfaces with fine-particle-fractions < 12% were found to be easily erodible.

Several studies used portable wind tunnels to investigate dust emission from crusted surfaces under different conditions in the field: Gillette et al. (1982) tested a range of crusted soils in undisturbed and disturbed (through driving of a pick-up truck) state and observed that only soils that had loose sand or pellet-sized material present were eroded in undisturbed state at regular friction velocities. Gillette et al. also characterized the crust morphological and compositional properties, including modulus of rupture, thickness, as well as clay, calcium carbonate, water soluble material, and organic matter content. Houser and Nickling (2001a, b) found PM10 (particulate matter with diameter $\leq 10\,\mu$m) dust emissions to be continuous when introducing sand abraders into their wind tunnel, but to decay rapidly after an initial peak without. Houser and Nickling found abrasion efficiency to depend on the ability of the sand to abrade the surface, which the authors related to particle momentum flux, and the susceptibility of the surface to abrasion, i.e. crust strength, determined using a hand penetrometer. In their experiments, surface disturbance did not necessarily lead to elevated PM10 levels as increased surface elasticity at disturbed patches can reduce particle rebound velocity. In contrast to the results from Rice and McEwan (2001), Houser and Nickling saw an increase of abrasion efficiency with PM10 fraction in the crust. Macpherson et al. (2008) studied the importance of dust entrainment mechanisms in the supply-limited regime and the effect of disturbance on the mechanisms for a range of soil textural characteristics. Macpherson et al. found a stronger increase in emission rates after (controlled)

mechanical disturbance on clay-crusted surfaces than on non-cohesive surfaces, and no significant changes on salt-crusted surfaces. Similarly, abrasion efficiency was found to increase after disturbance for the non-cohesive and clay-crusted surfaces, but to decrease for the salt-crusted surfaces, and to be generally higher for supply-limited conditions. For several of their test sites, Macpherson et al. detected substantial dust emission concurrent with very low saltation fluxes and concluded that aerodynamic entrainment was an important emission mechanism. Baddock et al. (2011) tested the effect of disturbance of a crusted playa surface through cattle trampling on dust emitted aerodynamically and by saltation bombardment. Baddock et al. found that aerodynamic entrainment occurred for all tested degrees of disturbance, but of generally small magnitude. Dust PM10 levels obtained when introducing abrader sand were substantially higher and increased saltation bombardment efficiency was found for the strongest disturbance.

Only a few studies attempted to account for soil crust in parameterisations of dust emission using a correction function. Fryrear et al. (1998) computed a crust factor based on laboratory measurement from Hagen et al. (1992) to apply to their saltation flux estimate. Goossens (2004) compared measured and predicted horizontal and vertical sediment fluxes and related the discrepancy to crust strength, thereby obtaining a correction function. Crust strength was assessed using a torvane.

Here, we aim to address the following research questions:

1. Do field measurements of transported sediment show evidence for a change with time of the saltation bombardment (abrasion) efficiency at a given location under natural conditions (i.e. without artificial disturbance)?

2. Can dust emission from a crusted surface be reproduced using a physics-based dust emission scheme with appropriate scheme parameters and input?

3. Is the resulting choice of parameters supported by observations?

To investigate the above research questions, we use (a) detailed field measurements of the land-surface characteristics, horizontal and vertical sediment transport, and meteorological conditions; and (b) the physics-based dust emission parameterisation from Shao (2004).

2 Field measurements

Detailed event-based measurements were conducted at six sites in the northern Chihuahuan Desert in New Mexico, USA, between February 2016 and February 2017. Five of the six sites were located within the USDA-ARS Jornada Experimental Range and one site was located on a playa near Lordsburg (Fig. 1). The site locations were chosen such that they cover a range of surface conditions. Each site covered an area of approximately $60 \times 60\,\mathrm{m}^2$.

Site A is a silt loam soil playa surface (see Fig. 2 in Klose et al. (2017)). The soil texture classes given here were obtained based on samples of the top $1-2\,\mathrm{cm}$ soil layer analysed in wet dispersion using laser diffractometry. The site had a stable physical and cyanobacterial crust and sporadic grass cover (see also Appendix A). Site B has a loamy soil texture. The site had little shrub/grass cover and a hard crust which was partly disturbed by cattle. Apart of the loose soil material arising from crust disturbance, a small amount of sand particles was present at the site originating from small nearby dunes. Site C has

Table 1. Site coordinates (locations of the meteorological towers) and soil texture based on analysis in wet dispersion.

Site	Latitude [Degrees North]	Longitude [Degrees East]	soil texture
A	32.534934	-106.719017	silt loam
B	32.578110	-106.675284	loam
C	32.608660	-106.730221	sand
D	32.569075	-106.760451	sand
E	32.712469	-106.828505	silty clay loam
F	32.325603	-108.871836	loam

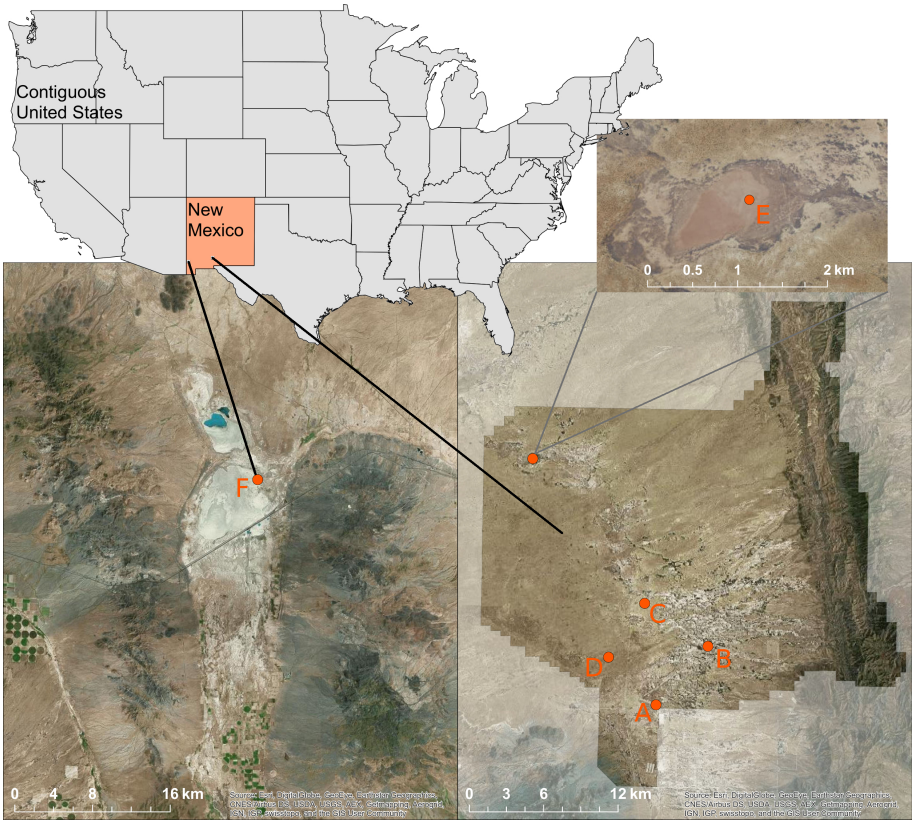

Figure 1. Locations of the six sites used in this study. Sites A-E are located within the Jornada Experimental Range (bottom-right) and Site F is located on the Lordsburg Playa. Site coordinates are given in Table 1. Map sources: Esri, DigitalGlobe, GeoEye, Earthstar Geographics, CNES/Airbus DS, USDA, USGS, AEX, Getmapping, Aerogrid, IGN, IGP, swisstopo, and the GIS User Community.

a sandy soil texture. Part of the site was dominated by loose erodible material, while other parts had a relatively weak, thin crust, which itself showed some patchy sand cover. Site C had some shrub and grass cover. Site D has sandy soil (coarser than

Site C), moderate shrub and grass cover and only little very weak crust, although more crust cover was present after winter rainfalls. More detail about the geographical settings of Sites A through D can be found in Webb et al. (2016) (their sites 2 to 5). Site E is located in an ephemeral lake and its surface is weakly crusted, not well-consolidated, of silty clay loam texture, and has essentially no vegetation. Site F is a distinct arcuate feature on the northeast shore of the main Lordsburg Playa in far southwest New Mexico. While crust hardness varies throughout Lordsburg Playa, the crust at Site F was very weak and thin. The soil texture class at Site F is loam and, as Site E, the site had close to zero vegetation. Fig. 2 shows the six sites. The site coordinates and soil textures are listed in Tab. 1.

The measurements were designed to provide insights into the physics of dust emission and included sampling of the top soil-layer, surface crust, and loose erodible material (LEM), sampling of the sediment transported in saltation, monitoring of the land-surface condition, meteorological measurements, and measurements of dust aerosol. No crust strength measurements were conducted. Initial tests using a pocket penetrometer with a punch diameter of several millimeters showed inconsistent results in particular for the sites covered by a very weak crust. The suitability of penetrometers with such large punch diameters for use in the context of wind erosion was questioned by Rice et al. (1997). In their study, crust strength measurements obtained using (a) a penetrometer with a flat-ended cylindrical punch of 6 mm outer and 5 mm inner diameter and (b) a penetrometer with a flat-tip stainless steel lace pin of 0.6 mm were substantially different, the magnitude of the difference being related to aggregate size. Rice et al. (1997) concluded that "these results demonstrate clearly that strength tests that are not on a scale comparable to the size of saltating particles are unlikely to be of use in comparing the erodibility of different surfaces". A penetrometer with such a fine tip was not available to us during the field measurements. Instead, we infer crust erodibility and changes in erodibility from observed sediment transport and application of a mathematical model.

2.1 Sediment sample collection and analysis

Information about the condition of the land-surface, including the availability of particles available for entrainment, and characterisation of the surface sediment and transported sediment is crucial to interpret sediment flux measurements at a location. Land-surface cover was monitored for each event using the line-point-intercept (LPI) method (see Appendix A for more detail). To characterise the surface sediment, samples of the top $\sim 1-2\,\mathrm{cm}$ soil-layer, the surface crust, and LEM were collected using simple random sampling. Apart from a few exceptions at an early project stage, samples were collected at nine random points per site and were composited in groups of three, resulting in three final samples per site for each sample type. Soil samples were collected once per site using a scoop. Crust samples were taken between one and three times per site and were obtained by removing pieces of the surface crust using a knife. Loose material on top of a collected crust piece was removed by tipping the crust piece if it was not too fragile. LEM samples were collected using the vacuum system developed by Klose et al. (2017). The system was designed to collect LEM samples representative of the material (both sand and dust) exposed to wind forces. The collection of transported sediment samples using passive MWAC samplers (Wilson and Cooke, 1980; Kuntze et al., 1990) is described in Section 2.2.

Volumetric particle-size analyses were performed for all soil, crust, LEM, and MWAC samples in the Arid Environments Laboratory at the University of Texas, El Paso, using a Malvern Mastersizer 2000 laser diffractometer (Malvern Instruments

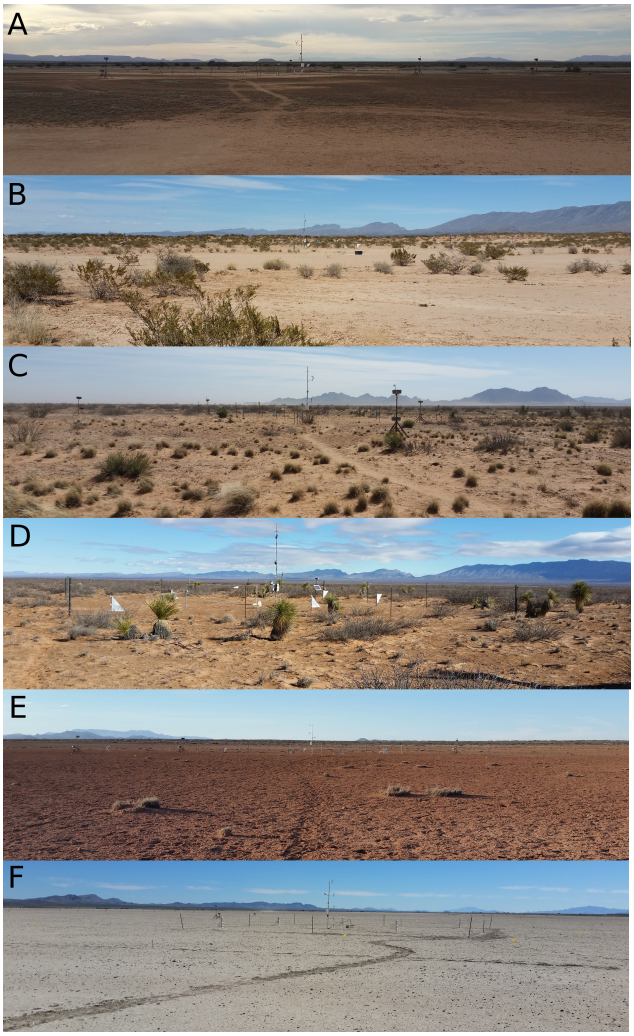

Figure 2. Photos showing the field sites and their surrounding.

Ltd., Worcestershire, UK) with the Scirocco 2000 accessory for sample dispersion in air (minimal dispersion) and the Hydro 2000 accessory for wet sample dispersion (full dispersion). Sample preparation and procedures for wet analyses followed protocols recommended by Sperazza et al. (2004) and Zobeck (2004). Analyses were conducted in triplicate using $\sim 1-3$ g of sample material each for the dry analyses and between 0.2 and 1.5 g (to reach appropriate laser obscuration) for the wet analyses. For some of the MWAC samples, the mass available was limited and the analysis aliquots were reduced accordingly in these cases. One hundred logarithmically-spaced particle-size bins from 0.02 to 2000 μm were used to assess the particle-size distributions (PSDs). Before conducting the particle-size analyses, the LEM, soil, and crust samples were passed through a 2 mm sieve. Soil and crust samples were forced through the sieve, i.e. soil aggregates larger than 2 mm were dispersed, while LEM samples were not. For the latter, any constituents larger than 2 mm were removed from the samples to avoid altering the

Figure 3. Measurement setup for Site C.

PSD of LEM below 2 mm. This procedure might have affected the dry soil-sample PSD. Crust samples were analysed in wet dispersion only, for which the sieving procedure is expected to have negligible effect.

2.2 Meteorological and sediment transport measurements

All sites were equipped with a 5 m meteorological tower holding cup-anemometers and temperature sensors at different heights and a wind vane (see Appendix B for more detail). Measurements of sediment transport were taken using a Wenglor® optical gate sensor (model YH03PCT08, 655 nm laser and photosensor 30 mm apart) at 5 cm height, a Big Spring Number Eight (BSNE) sediment sampler located above the Wenglor at ~ 25 cm height, five rotating masts each holding Modified Wilson and Cooke (MWAC) samplers at four heights (10, 25, 50, and 85 cm) and up to three pairs of TSI DustTrak™ aerosol monitors (model 8520), each pair consisting of one DustTrak at approximately 1 m and one at 2 m. Two SANTRI® (Standalone AeoliaN Transport Real-time Instrument) platforms (Etyemezian et al., 2017; Goossens et al., 2018) were available additionally for some of the measurement episodes. The SANTRI consists of duplicate optical gate devices (Etyemezian et al., 2017) at heights of 5 and 30 cm, anemometer and wind vane at 1 m, and temperature and relative humidity sensors at 0.7 m (heights can be varied and are given as used in the present study).

Figure 3 shows the measurement setup for Site C. The tower was located in the approximate site center with the Wenglor and BSNE close to it. MWAC masts were distributed over a centered $20 \times 20\,\mathrm{m}^2$ area, while the DustTrak pairs were positioned at random locations outside of the center area, one each within 60°-sectors of an imaginary circle covering the site to achieve

areal coverage. SANTRIs were placed across the site and locations were varied by event. The reason for the interior $20 \times 20\,\mathrm{m}^2$ area is of practical nature – four of the six sites (A-D, see Sec. 2) included permanently installed and instrumented (tower, MWACs, BSNE, Wenglor) $20 \times 20\,\mathrm{m}^2$ sites which were utilized for this study. We therefore supplemented those sites with DustTraks outside of the region with permanent instrumentation and replicated the entire setup at sites E and F for consistency.

Appendix B details how the collected meteorological and sediment transport data were used to calculate friction velocity u_*, convective scaling velocity w_*, streamwise saltation flux Q, and dust emission flux F.

3 Field measurement results

Measurements were conducted for 17 events between Feb 2016 and Feb 2017. Most measurement periods were conducted on Site C (6 of 17). Measurement episodes on Site C all experienced relatively high u_* (between 0.7 and $1.0\,\mathrm{m\,s^{-1}}$) and sediment transport was overall among the highest of all the sites. Sediment transport events at the other sites were either comparatively minor (Sites A, D, and E) or were too few in number to enable inter-event comparisons (Sites B and F).

In the following, we focus on Site C (expansion of Site 4 in Webb et al. (2016)). Site C had a sandy soil texture and moderate heterogeneous shrub and grass cover (Section 2). The site surface was dominated by loose sand and a patchy and weak crust. While only $\approx\ 8\%$ of the site's surface were recorded as crusted according to LPI (see Appendix A), a substantial area fraction of the site, particularly in the site centre, showed a surface crust, but overlaid by a thin layer of LEM, thus preventing it from being captured by LPI. The combination of a weak, erodible crust and the loose sand present on the site makes Site C an efficient dust source. Due to large sand deposits especially at the site fringes and around, saltation during dust events was relatively continuous.

3.1 Observed dust events on Site C

Substantial sediment transport was observed during all six measurement days on Site C. On 12 March, strong winds and first dust emissions occurred in the morning, followed by a period of lower dust activity during noon and intense emissions and severe visibility reductions in the area during the afternoon. Fig. 4 shows u_*, u_{*t}, and w_* as well as Wenglor saltation counts and dust concentration for the six measurement episodes on Site C. During the next observation period on 14 March, dust emissions were observed mainly in the afternoon and remained less intense than two days before. On 22 March, local dust emissions were observed starting around noon, dust was initially lifted from the walking path to the site center, then from other areas on the site as well as at places in its proximity. Dust devils were also observed in some distance. Sediment transport intensified during the afternoon and considerable dust haze was present in the afternoon (around 16:20 LST), which is confirmed by a peak in dust concentration at about that time. Dust was still actively emitted after 18 LST, at which time the dust monitoring equipment had to be taken down. On 23 March, local events again started around noon, but intensified more quickly with strong dust emissions shortly after. Dust emissions ceased during the afternoon, but resumed later and continued until the evening. Peak dust concentrations of about $5\,\mathrm{mg\,m^{-3}}$ were reached on this day. It was visually apparent in the evening of March 23rd that the surface crust had been abraded.

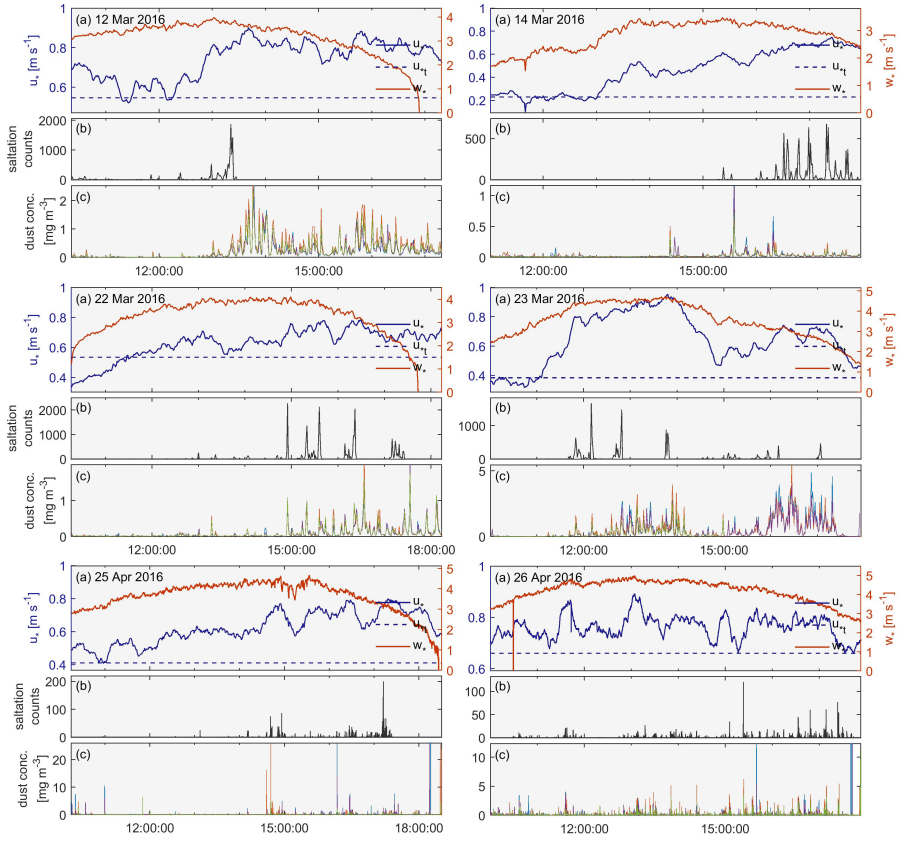

Figure 4. (a) Friction velocity u_*, threshold friction velocity u_{*t}, and convective scaling velocity w_* (all in [m s^{-1}]), (b) Wenglor saltation counts, and (c) dust concentration [mg m^{-3}] for the six dust measurement periods on Site C.

On 25 April, dust emission started in the afternoon with two local micro-events on site following closely upon one another. After that, emission remained active almost continuously until the evening of 26 April. Due to the strongly unstable atmospheric stratification (as suggested by large w_*; w_* was between 3 and 5 m s^{-1} during most of both days) and despite or maybe supported by the strong wind shear (indicated by large u_*), several dust devils were generated and observed in some distance to the site around and after 15 LST. Saltation was active continuously during the afternoon and evening of 25 April and during most of the day on 26 April. As a consequence, ripples were detected late on 26 April at the downwind part of the site, where large sand deposits existed. Substantial dust concentrations were recorded throughout both days. Dust emissions were mostly under $\sim 300\,\mu g\,m^{-2}\,s^{-1}$, but peaked to $\sim 600\,\mu g\,m^{-2}\,s^{-1}$ early on 25 April (cf. Fig. 9).

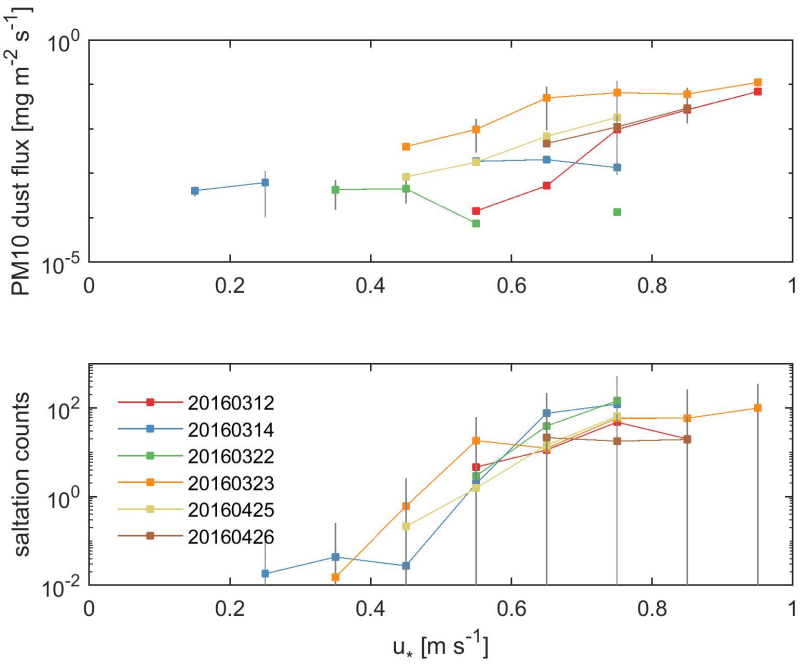

Figure 5. Average (a) dust emission flux, F [mg m^{-2} s^{-1}] obtained from DustTrak measurements and (b) Wenglor® saltation counts versus friction velocity, u_* [m s^{-1}], for 6 events in spring 2016 on Site C. Colors indicate the measurement date (format yyyymmdd). Grey vertical lines indicate the standard deviation.

3.2 Sediment transport

Fig. 5 shows 1-min saltation counts and dust emission flux, F [mg m^{-2} s^{-1}], that have been averaged over intervals of friction velocity, u_* [m s^{-1}], for the six events on Site C. On 14 and 22 March, F was smaller compared to 12 March for large u_*, despite a larger number of saltation counts. A possible reason for that is the strong previous event on 12 March, during which the surface had been eroded, which was visually evident on the evening of 12 March. Assuming that the least stable surface areas are eroded first, the post-event surface was likely more consolidated, resulting in reduced dust emission during the event two days later.

On 23 March, dust emissions were again strong, most likely due to a change in wind direction by $\sim 70°$ from southwesterly to northwesterly, which could have released sediment previously accumulated around roughness elements, thereby exposing different surface areas to saltation and the soil crust to particle impacts from a different direction. On 25 and 26 April, dust emissions remained strong. Note that the saltation counts shown here need to be interpreted with caution due to gaps in the Wenglor records due to clogging of the laser window (cf. Fig. 4). The Wenglor optical sensors were regularly cleaned during the measurement episodes to avoid particles adhering to them, which is a known problem (Hugenholtz and Barchyn, 2011). It was found, however, that cleaning would have been required more often as the records suggest that clogging occurred sometimes

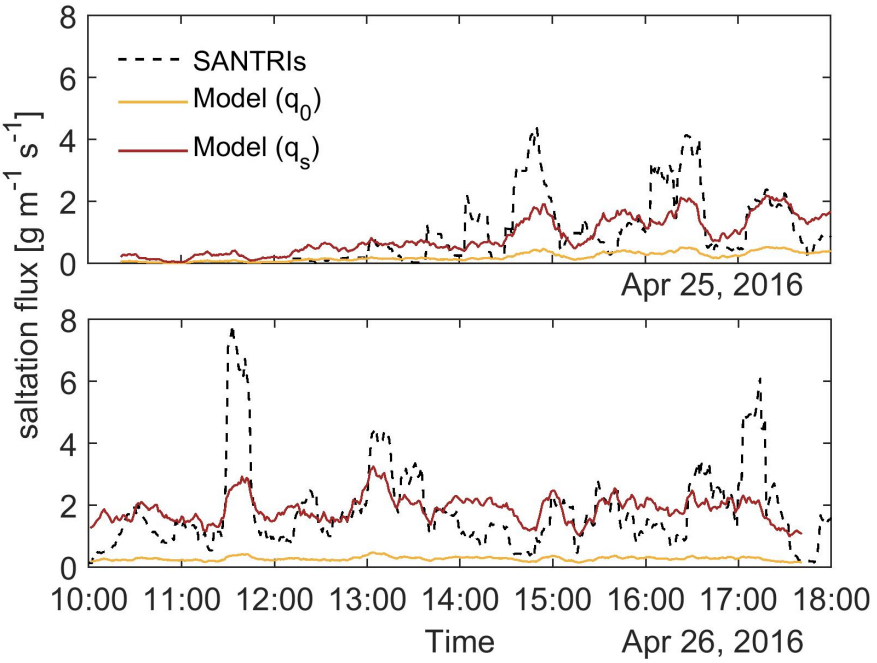

Figure 6. Saltation flux obtained from SANTRI measurements (black dashed line) on 25 April (top) and 26 April (bottom) and saltation flux estimated based on Kawamura (1964) (with $c_0 = 7.6$) and scaled with q_s (red line) and q_0 (yellow line). Scaling factors were obtained as described in Section 4.1.1.

only few minutes after cleaning. The relatively large standard deviations of the saltation counts for large u_* in Fig. 5 might in part be caused by zero-counts due to clogging. For that reason, we are mainly relying on MWAC and SANTRI saltation data in this paper.

Only little rainfall occurred on the site in March and April 2016: 0.25 mm on 14 March at 09:47 LST; 2 mm on 08 April during the first half of the day; 2.25 mm on 12 April between about 11 and 14:30 LST; and 0.25 mm in the evening of 22 April. Precipitation has therefore likely had negligible effects on the observed variation in sediment transport rates.

Time-resolved saltation flux is available from SANTRI measurements (cf. App. B) on 25 and 26 April and is shown in Fig. 6. Times of large Q coincide generally with times of large F (compare Fig. 9), confirming that local, saltation-based dust emission occurred. Except for a few individual peaks, saltation flux was typically smaller than 3 g m^{-1} s^{-1} on both days.

4 Combining observations with insights from a dust emission scheme

Existing dust emission schemes are not well tested for dust emission from crusted soils. Here, we want to test the capability of a state-of-the-art dust emission scheme to reproduce the observed dust emissions. For this purpose, we selected the parameterisation from Shao (2004). The scheme is physics-based and estimates size-resolved dust emission based on the soil volume

removed by saltation impacts. This concept seems particularly suitable to represent crust abrasion through saltation grain impacts. The scheme is described in detail in Shao (2004) and Shao et al. (2011) and we encourage the reader to read the original papers for details on the scheme physics. Here, we only briefly highlight and discuss the aspects relevant for this study.

In the scheme of Shao (2004), the flux of dust particles of diameter d_i, emitted by saltators of size d_s is given as

$$F(d_i, d_s) = (1 - f_F)\, c_y \eta_{fi} \left[(1-\gamma) + \gamma\sigma_p\right] \times (1 + \sigma_m) \times \frac{Qg}{u_*^2} \tag{1}$$

where c_y is a coefficient, η_{fi} is the mass fraction of dust with diameter d_i in fully dispersed particle-size analysis, σ_p is the free dust to aggregated dust ratio, and g is gravitational acceleration. γ represents the aggregate binding strength and is given as

$$\gamma = \exp\left[-\kappa\left(u_* - u_{*t}\right)\right]. \tag{2}$$

κ is a coefficient that represents aggregate stability (larger κ means less stable). u_{*t} was calculated for smooth and dry conditions based on Shao and Lu (2000) and then corrected for the presence of vegetation cover following Raupach et al. (1993). For this purpose, we converted the vegetation cover fraction obtained through LPI to a frontal area index using a simple logarithmic relationship as suggested by Shao et al. (1996). The parameters required by the drag partition scheme of Raupach et al. (1993) were set as $\sigma = 1$ (basal to frontal area), $m = 0.5$ (coefficient), and $\beta = 90$ (ratio of frictional and pressure drag coefficients), the latter being on the lower edge of values recommended and discussed by Shao et al. (2015). Some uncertainty is related to the choice of parameter values (see Shao et al., 2015, and references therein), which might have an effect on our results. However, we do not expect strong effects, because the variation of vegetation cover between events on Site C was small (see Fig. A1) and because we applied a scaling to the modelled saltation flux to match the observed magnitude (see Sec. 4.1.1).

σ_m is the saltation bombardment efficiency estimated as

$$\sigma_m = 12 u_*^2 \frac{\rho_p}{P}\left(1 + 14 u_* \sqrt{\frac{\rho_p}{P}}\right) \tag{3}$$

with soil bulk density ρ_p [kg m^{-3}] and soil plastic pressure P [N m^{-2}]. The total saltation flux, Q is obtained as particle-size weighted average of the size-dependent saltation flux $Q_d(d_s)$,

$$Q = (1 - f_Q) \int_{d_1}^{d_2} Q_d(d_s)\, p_s(d_s)\, \delta d, \tag{4}$$

where $Q_d(d_s)$ varies with u_* and is obtained from Kawamura (1964) (with coefficient $c_0 = 7.6$ as used by Shao et al., 2011). The interval $[d_1, d_2]$ defines the saltation particle-size range. A heuristic approach to adapt Q for the conditions considered here is discussed in Section 4.1.1. The saltation particle-size distribution is estimated combining the minimally and fully dispersed PSDs of the parent soil (see Section 4.1.3),

$$p_s(d_s) = \gamma p_m(d) + (1-\gamma)\, p_f(d). \tag{5}$$

The factors $(1 - f_F)$ in Eq. 1 and $(1 - f_Q)$ in Eq. 4 account for areas from which no entrainment is possible (e.g. Darmenova et al., 2009). Here, f_F is the cover fraction of vegetation, litter, and gravel, and f_Q additionally includes crusted areas without LEM.

4.1 Scheme input related to crusted surfaces

Key input quantities for the dust emission scheme in the context of crust abrasion are the parameters c_y, κ and P, the minimally and fully disturbed PSDs, as well as the saltation flux Q. In the following, we approximate Q and optimize the parameters and PSDs for the conditions of our study site to obtain the most suitable combination. We then evaluate and interpret the results based on the observational insights.

4.1.1 Saltation flux

Parameterisations of horizontal saltation flux describe saltation as a self-limiting process determined by the equilibrium between atmospheric momentum supply and particle momentum absorption (Shao, 2008, and references therein). A prerequisite condition for these parameterisations is the unlimited availability of particles for saltation. This condition is not given in the case of crusted surfaces and application of classic saltation-flux parameterisations is therefore problematic.

The availability of material for saltation on our test site C is relatively large despite the presence of a crusted surface (cf. Section 3). We therefore expect the observed saltation flux not to deviate too much from the predicted flux in terms of its temporal evolution, but to be of smaller magnitude. A comparison between the saltation flux obtained using the SANTRI counts for two dust episodes, Q_{obs}, and estimated using the parameterisation of Kawamura (1964), Q_{mod}, confirms this presumption (Fig. 6). Shown in Fig. 6 are Q_{obs} and $q_s \cdot Q_{\text{mod}}$, with q_s being a scaling factor obtained through linear fitting with Q_{obs}. Modelled (including the scaling) and observed values agree relatively well, with discrepancies for individual peaks, which was expected given the heterogeneous surface conditions. While this approach does not correctly represent the physics of the saltation process under the given conditions, it serves well to obtain an estimate of Q, which is needed as an input to the dust emission parameterisation. The development of a parameterisation for saltation under supply-limited conditions is a matter of current research (e.g. Selmani et al., 2017) and is beyond the scope of this paper.

As SANTRI measurements are only available for two of the six measurement periods on Site C, we also computed a q_0 through comparison of Q_{mod} averaged over the measurement duration with that obtained from the MWAC samples. The advantage of using the MWAC samples is that they are available for all events, but a disadvantage is that the MWAC data does not allow for a temporal evaluation during an event. The scaling factor obtained from MWAC event-integrated Q was larger than that obtained from SANTRI data for 25 and 26 April (resulting in a smaller modelled saltation flux, cf. Fig. 6), but of similar magnitude for 12, 22, and 23 March and somewhat larger for 14 March (Table 2). We have therefore decided the use the MWAC-based q_0 for 12 – 23 March and the SANTRI-based q_s for 25 and 26 April. We are using individual scaling for all events rather than an average value to allow accounting for the possibly different availability of sand particles.

4.1.2 Aggregate stability and soil plastic pressure

Aggregate stability, κ, determines "how rapidly γ approaches zero as u_* increases, and hence $p_s(d)$ approaches $p_f(d)$" (Shao et al., 2011). The larger the value of κ is, the easier a soil is disaggregated. For soils that contain only a very small amount of particle aggregates, i.e. soils that have similar/equal p_m and p_f, κ has no effect. Shao et al. (2011) tested the sensitivity of the

Table 2. Scaling factors for modelled saltation flux obtained through comparison with MWAC and SANTRI (where available) measurements.

Date	MWAC	SANTRI
12 Mar 2016	149.5	NA
14 Mar 2016	470.3	NA
22 Mar 2016	129.7	NA
23 Mar 2016	132.3	NA
25 Apr 2016	650.3	156.3
26 Apr 2016	1080.6	157.6

scheme to κ and found it relatively insensitive when varying κ between 0 and 1 given the observed friction velocities, which were mostly below $0.5\,\mathrm{m\,s^{-1}}$. Their test site had sandy loam texture (when using a sample dispersion technique similar to the one used in our study) and a relatively uniform and loose surface. It is likely that a stronger effect becomes visible for greater friction velocities. Here, we test the following values of κ: 0.1, 0.2, 0.3, 0.5, 0.7, 1.0, 1.2, 1.5.

Soil plastic pressure, P, is the pressure, or (shearing) force per area, that – when applied to the soil – causes its deformation. It is therefore a measure of how resistant a soil surface is to abrasion through saltation impacts. Combining P with soil bulk density, ρ_b, Shao et al. (2011) introduced a scaling velocity, u_{*P}, defined as $u_{*P}^2 = P/\rho_b$. Different values for P were reported in the literature. Goossens (2004) measured values between 12 and 34 kPa using a torvane on an agricultural field in northwestern Germany, but note that values for weak and very weak crusts are missing in their data and that extrapolation to smaller values is problematic. Zimbone et al. (1996) reported a shear strength value of 10 kPa for a crusted sandy loam soil. Most applicable in the context of a saltation-process based parameterisation are probably the values reported by Rice et al. (1997) due to the small pin diameter of the penetrometer they used (see Section 2). For soils with fine and medium-sized aggregates (< 2 mm), Rice et al. (1997) reported maximum penetration pressures between 5.1 and 32.6 kPa when the soil crust was generated through spraying, and between 14.5 and 1,637 kPa when the soil crust was obtained through tension wetting. Rice and McEwan (2001) used the same penetrometer to assess crust strength for the surfaces tested in their wind tunnel, but only reported penetration energy and not pressure. Corresponding to a range for P of $1 - 1000$ kPa as reported by Rice et al. (1997), Shao et al. (2011) estimated a range for u_{*P} of $1 - 30\,\mathrm{m\,s^{-1}}$ assuming $\rho_b \sim 1000\,\mathrm{kg\,m^{-3}}$. Testing values of $u_{*P} = 3.5, 4.0, 4.5, 5.0$ and 5.5, which seemed most suitable for their test site, Shao et al. found the dust emission scheme to be moderately sensitive to u_{*P} with the degree of sensitivity depending on the ratio u_*/u_{*P}. Shao (2004) recommended generally smaller P for loose sandy soils and larger P for hard-crusted clay soils. In our study, we allow P to assume the following values: 1, 3, 5, 10, 20, and 30 kPa.

In addition to κ and P, we also vary c_y using values of 1, 2, 4, 6, 8, and 10×10^{-5} to find the best combination between the parameters. This range of c_y is as suggested by Shao (2004) and Shao et al. (2011). The best choice for the test site used by Shao et al. was $(5 \pm 1) \times 10^{-5}$.

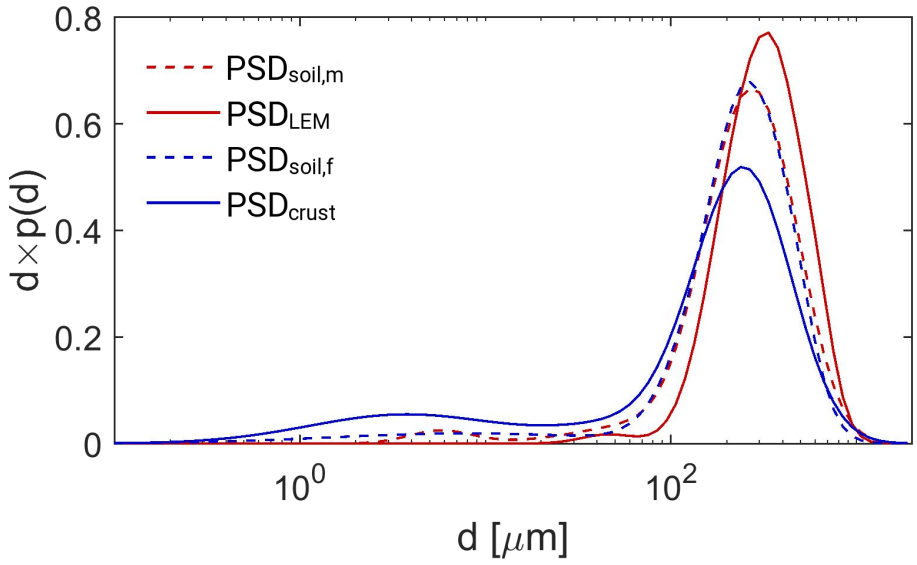

Figure 7. Particle-size distributions of the top 1-2 cm soil layer analysed in wet/dry dispersion ($PSD_{soil,f}$ and $PSD_{soil,m}$), loose erodible material analysed in dry dispersion (PSD_{LEM}), and soil crust analysed in wet dispersion (PSD_{crust}) as they are used as model input.

4.1.3 Particle-size distributions

To estimate size-resolved dust emission, the dust emission scheme requires information on the particle-size distribution of sediment transported in saltation as well as of the soil exposed to abrasion through saltating grains. Samples of the top ∼1–2 cm soil layer are typically used to obtain PSDs for use in dust models. Such PSDs might not be suitable to represent the particle population exposed to wind forces at the soil surface, as soil texture can vary even between the topmost millimetres due to, e.g., particle sorting. This is especially the case for crusted soils as the crust PSD is likely substantially different to that of LEM on top of the crust. The latter constitutes the particles initially available for lifting by wind forces.

In this study, we collected separate samples of the top 1–2 cm soil layer, the soil crust, and LEM (see Section 2.1) to investigate the difference between their PSDs and to evaluate effects of the different PSDs on the modelled dust emissions. Fig. 7 shows the PSDs obtained from the soil, crust, and LEM samples analysed in wet and dry dispersion. The Shao (2004) scheme makes use of a minimally and a fully disturbed PSD. The former represents the PSD obtained using dispersion weak enough not to break soil aggregates, while the latter describes the PSD of soil once all aggregates are broken (mechanically) into their constituents. Here, we use the PSDs analysed in dry and wet dispersion, respectively, to approximate the minimally and fully dispersed PSD.

The minimally and fully dispersed PSDs of the top soil layer, $PSD_{soil,m}$ and $PSD_{soil,f}$ are very similar (Fig. 7). Reasons for that are that the soil texture is sandy and contains only a small fraction of particle aggregates, and that the millimetre-thin surface crust is under-represented in a sample of 1-2 cm thickness. Furthermore, soil samples were passed through a 2 mm sieve before analysis (Section 2.1). This disaggregated most of the rather weak surface crust to some degree. Small differences

Table 3. Parameters used in Eq. 6 to reproduce $PSD_{soil,m}$, $PSD_{soil,f}$, PSD_{LEM}, and PSD_{crust}.

	p_1			p_2			p_3			p_4		
	w_1	$\overline{\ln d}_1$	σ_1	w_2	$\overline{\ln d}_2$	σ_2	w_3	$\overline{\ln d}_3$	σ_3	w_4	$\overline{\ln d}_4$	σ_4
$PSD_{soil,m}$	0.50	5.36	0.45	0.39	5.93	0.43	0.09	4.43	0.89	0.02	1.75	0.40
$PSD_{soil,f}$	0.48	5.60	0.42	0.32	5.18	0.52	0.12	6.11	0.30	0.08	2.10	1.71
PSD_{LEM}	0.66	5.56	0.44	0.26	6.03	0.31	0.07	6.43	0.21	0.01	3.82	0.33
PSD_{crust}	0.43	5.27	0.54	0.32	5.79	0.50	0.16	1.31	1.20	0.09	4.28	0.87

exist in the size-ranges $d < 3\,\mu$m and $d > 500\,\mu$m. In contrast, the PSDs of LEM analysed in dry dispersion, PSD_{LEM}, and soil crust analysed in wet dispersion, PSD_{crust}, are substantially different to each other and to both soil PSDs, which are intermediate to PSD_{LEM} and PSD_{crust} (Fig. 7). Here, we test PSD_{LEM} as alternative minimally dispersed PSD, representing the particles initially available, and PSD_{crust} as alternative fully dispersed PSD, representing the extreme limit of particles generated through abrasion.

In the model, the PSDs are reproduced as weighted sum of four log-normal distributions (e.g. Gomes et al., 1990; Shao, 2001) with predetermined parameters w_j, σ_j, and $\overline{\ln(d)}_j$ for each distribution p_j:

$$p_j(d) = \sum_{j=1}^{4} w_j \frac{1}{d\sqrt{2\pi}\sigma_j} \exp\left(-\frac{\left(\ln(d) - \overline{\ln(d)}_j\right)^2}{2\sigma_j^2} \right) \tag{6}$$

The parameters for the PSDs used here and shown in Fig. 7 are given in Table 3.

4.2 Dust emission flux – model and observations

In our first set of experiments, we used $PSD_{soil,m}$ and $PSD_{soil,f}$ as input to the dust emission scheme as it is common (see Section 4.1.3). The resulting temporal variation of the modelled dust emission flux F_{mod}, was too flat compared to the observations, even when optimizing κ and P. This is due to the small dust fraction in $PSD_{soil,m}$ and the similarity of both PSDs. Note also that κ had little effect on F_{mod} due to this similarity. As an example, Fig. 8 shows the results using $PSD_{soil,m}$ and $PSD_{soil,f}$ with the optimized parameters c_y, κ and P (the optimization procedure is described below).

Assuming that LEM determines the particles and particle aggregates available for saltation and that dust emission is dominated by crust abrasion, we replaced $PSD_{soil,m}$ with PSD_{LEM} and $PSD_{soil,f}$ with PSD_{crust} for our second set of experiments. Results showed that changing the PSDs had a large effect on F_{mod} and that the observed dust emission flux, F_{obs}, could be much better reproduced. The larger difference between the PSDs and the larger dust fraction in PSD_{crust} led to a stronger variation of F.

Most events were very well reproduced using the Shao (2004) scheme with appropriate input parameters and PSDs. Fig. 9 shows modelled and observed dust emissions using the optimal combination of c_y, κ, and P. The parameter combinations were ranked based on Pearson correlation coefficient and root-mean-square error (applied in this order) between model results and

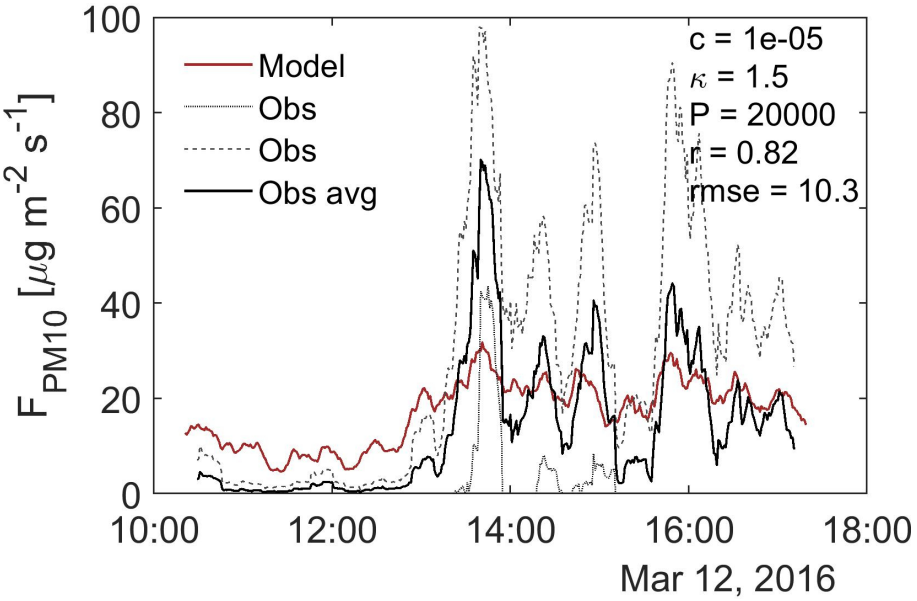

Figure 8. Modelled (red line) and observed (black line) dust emission flux, F [μg m^2 s^{-1}], obtained using optimized values for c_y, κ, and P [Pa], as well as PSD$_{\text{crust}}$ and PSD$_{\text{LEM}}$. The observed F is taken as the average of F from each instrument-pair passing the quality control (colored dashed lines, see Section B for details on the quality control). Pearson correlation coefficient, r, and root-mean-square error, rmse [μg m^2 s^{-1}], are indicated in the figure. The temporal evolution of F is too flat compared to the observations when using PSDs of the top 1–2 cm soil layer as scheme input.

observations. Very good agreement could be achieved for the events on 12 March, 23 March, 25 April, and 26 April 2016. On 12 March, model and observations agree very well during the whole measurement period with only individual peaks/sinks being slightly under-/overestimated. Exceptional agreement was achieved for the first half of 23 March 2016. During the second half of the day the observed two peaks were clearly underestimated. Note that records from only one instrument pair are available for the afternoon of 23 March due to instrument failures, which makes reproduction of the observations using a model more difficult, because localized effects receive stronger emphasis. For that reason, parameters for 23 March were determined using data for the first half of the day only (until 14:30 LST). Both 25 and 26 April show generally good agreement between model and observations, with discrepancies for particular times, for example at about 15 LST on 25 April and about 15:45 LST on 26 April. For 14 and 22 March, observed dust emissions could not be reproduced satisfactorily. While the temporal evolution could be matched to some degree on 22 March, the peak in dust emission flux on 14 March was predicted much later than observed. This was surprising given that both observed u_* and Wenglor saltation counts suggested the maximum dust emission to occur past 17 LST rather than earlier in the afternoon as visible in the observed F. Observed u_* is input to the dust emission scheme and caused the late peak in modelled F. It is possible that advection played a role on 14 March, causing the mismatch between observations and model results. The dust emission flux F inferred here using the gradient method (Gillette et al., 1972, see also App. B) is sensitive to small changes in measured dust concentration. In the gradient method, a steady-state and

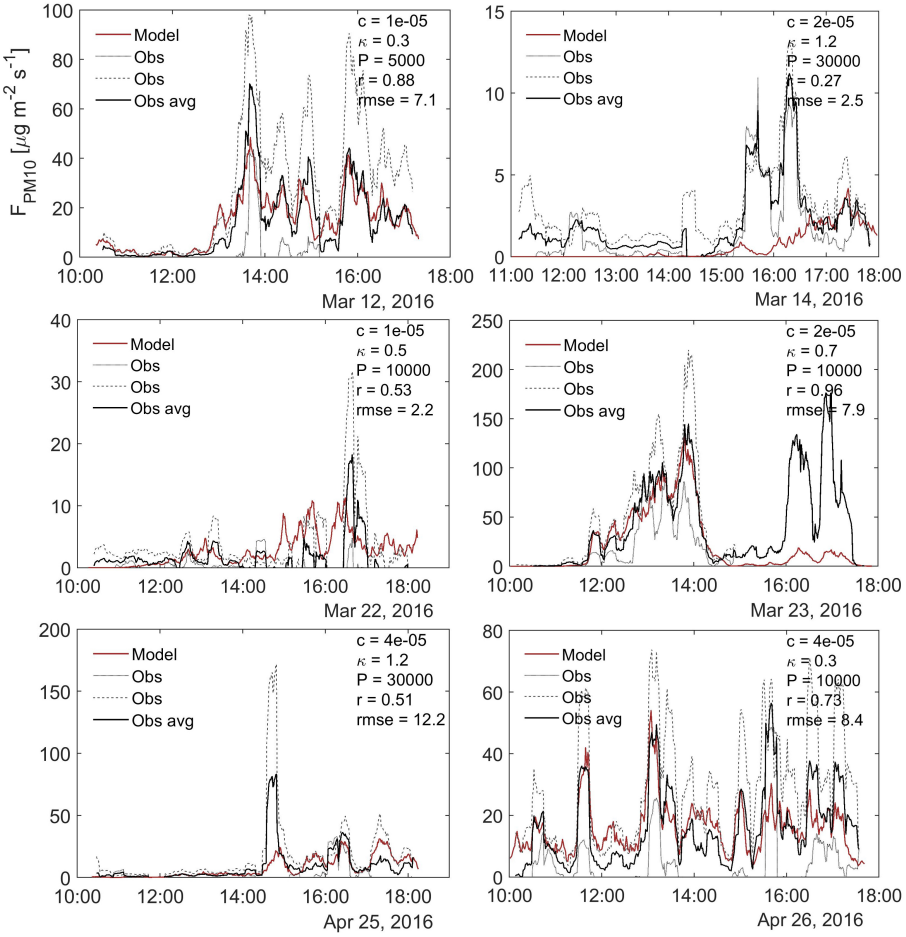

Figure 9. Modelled (red line) and observed (black line) dust emission flux, F [μg m^2 s^{-1}], obtained using optimized values for c_y, κ, and P [Pa], as well as PSD$_{\text{crust}}$ and PSD$_{\text{LEM}}$. The observed F is taken as the average of F from each instrument-pair passing the quality control (colored dashed lines, see Section B for details on the quality control). Pearson correlation coefficient, r, and root-mean-square error, rmse [μg m^2 s^{-1}], are indicated in the figure. Note that parameters as well as r and rmse for 23 March 2016 were determined using the first half of the day (until 14:30 LST) only.

horizontally homogeneous dust concentration field is assumed (Shao, 2008). Discrepancies to these assumptions can lead to elevated F-estimates that might not be related to actual surface emissions and hence cannot be reproduced by a dust emission scheme. Such discrepancies are likely to have contributed to the observation-model differences on 14 and 23 March.

While the optimal values identified using statistical means are informative, a number of different combinations yield results of similar (statistical) quality. It is therefore useful to consider also parameter combinations that provide satisfactory results, but that are not the top-choice combination. We therefore simplify the situation by keeping the tuning coefficient c_y constant

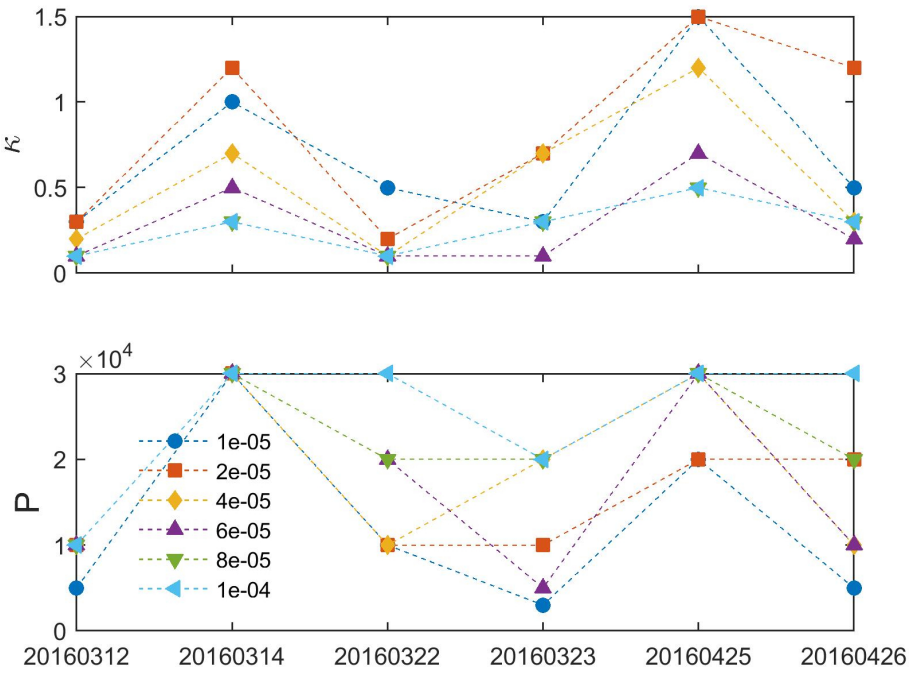

Figure 10. Optimal combinations of parameters c_y, κ, and P [Pa] based on Pearson correlation coefficient and root-mean-square error obtained from comparing F_{mod} and F_{obs} for each event on Site C. c_y is held constant and indicated in the legend.

while varying κ and P. Fig. 10 summarizes the best combinations of c_y, κ, and P for each of the events, when c_y is held constant.

Both κ and P have a similar pattern of change between the events. The optimal values tend to be relatively small on 12 March, followed by larger values on 14 March. On 22 March, P remains large for the largest c_y, while for others it drops again like κ does. For 23 March, 25 April, and 26 April, values alternate between relatively smaller and larger values. More confidence should be given to the parameters obtained for the events for which model and observations agree well. For events that could not be reproduced well, e.g. 14 March, the quality indicators are likely not very meaningful and parameters have substantial uncertainty. Table 4 summarizes the optimal values for κ and P with constant $c_y = 6 \times 10^{-5}$ together with those obtained for varying c_y as given in Fig. 9. Time series of modelled dust emissions with the optimized values for constant c_y as listed in Tab. 4 are almost identical to those shown in Fig. 9 and are therefore not repeated here.

As κ defines the degree of disaggregation during wind erosion, it affects the amount of dust released for a given u_*. A smaller κ leads to a larger increase of F with u_*. P scales the part of F that is due to saltation bombardment (cf. Eq. 1) and smaller values of P lead to larger σ_m (saltation bombardment efficiency). Assuming $c_y = 6 \times 10^{-5}$, similar to the value recommended by Shao et al. (2011), Fig. 10 suggests that on 23 March, 12 March, and 26 April, the strongest increase of F with u_* and the largest relative emissions were observed given the small values for both κ and P. Somewhat smaller fluxes are expected for 22 March due to the larger P. On 14 March and 25 April, the increase of F with u_* is expected to be more shallow and

Table 4. Optimized parameters κ and P [Pa] for varying and for constant c_y, together with Pearson correlation coefficient, r, and root-mean-square error, rmse [μg m^2 s^{-1}].

Event date	c_y	κ	P	r	rmse	c_y	κ	P	r	rmse
12 Mar 2016	1×10^{-5}	0.3	5000	0.88	7.1	6×10^{-5}	0.1	10000	0.88	7.7
14 Mar 2016	2×10^{-5}	1.2	30000	0.27	2.5	6×10^{-5}	0.5	30000	0.27	2.5
22 Mar 2016	1×10^{-5}	0.5	10000	0.53	2.2	6×10^{-5}	0.1	20000	0.53	2.2
23 Mar 2016	2×10^{-5}	0.7	10000	0.96	7.9	6×10^{-5}	0.1	5000	0.96	8.4
25 Apr 2016	4×10^{-5}	1.2	30000	0.51	12.2	6×10^{-5}	0.7	30000	0.51	12.3
26 Apr 2016	4×10^{-5}	0.3	10000	0.73	8.4	6×10^{-5}	0.2	10000	0.73	8.4

fluxes lower based on the estimated smaller parameter values for κ and P. Fig. 11 shows the relationship between modelled F (PM10), Q, and F/Q with u_*. Note that the ratio F/Q is different to the bombardment efficiency σ_m in Shao (2004). The plots confirm the described theoretical behaviour based on the parameter estimates. The strongest increase of F with u_* is found for 23 March, followed by 26 April and 12 March. 14 and 22 March show weaker increases. The ratio F/Q, which illustrates the relative change of F for a given Q, suggests that relative emissions were largest on 23 March, followed by 26 April and 12 March. Large relative emissions are also shown for 25 April and 14 March, in particular for relatively smaller u_*. F/Q is smallest for 22 March. The results for 25 April deviate somewhat from the expected behaviour for both F and F/Q. This is possibly due to a discrepancy between the modelled and observed saltation fluxes (compare Fig. 6). Results for 14 April also need to be interpreted with caution given the unsatisfactory agreement between model results and observations for this event as discussed before. Comparison with observed saltation counts (Fig. 5) confirms a good qualitative agreement between modelled and observed saltation with some discrepancies for 14 March, 22 March, and 25 April. Also the expected behaviour of F based on the parameter estimates and illustrated in Fig. 11 is confirmed to large degree by the observations shown in Fig. 5. The results demonstrate that the observed temporal variability in dust emission efficiency (as shown in Fig. 5) can be reproduced through variations in parameters related to crust erodibility, i.e. κ and P, in the dust emission scheme of Shao (2004).

5 Conclusions

In this study, we combined field measurements and numerical modelling to investigate dust emission from a crusted surface. Our results showed that the dust emission parameterisation from Shao (2004), which parameterises dust emission based on the soil volume ejected by saltation impacts, is suitable to predict dust emission from crusted surfaces using existing model parameters, i.e. without addition of a separate function representing the soil crust. A necessary prerequisite condition is, however, that scheme input is specified adequately. Here, we showed that using PSDs of LEM and soil crust, rather than the top soil layer, can substantially improve numerical dust emission estimates for crusted conditions. Using the improved PSD information, scheme parameters used to characterise the soil surface condition, i.e. aggregate stability and soil plastic pressure, were

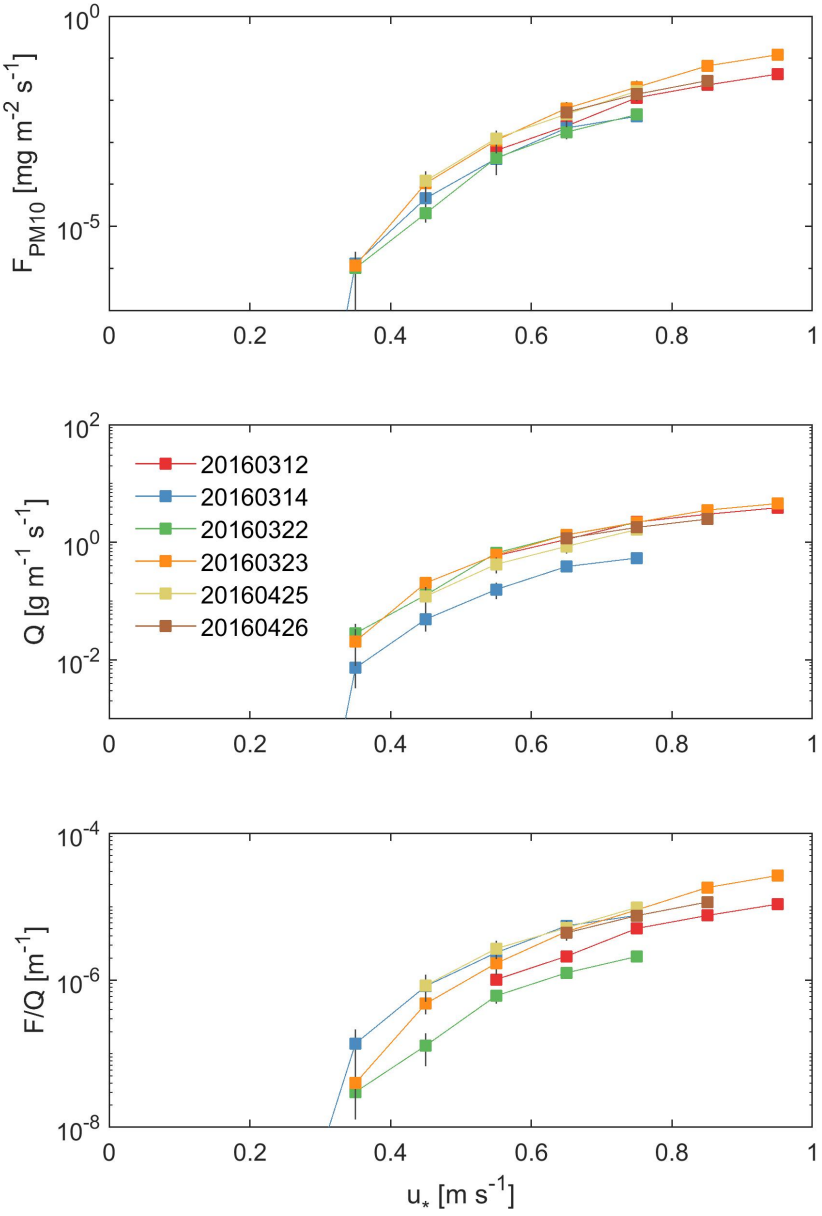

Figure 11. Relationship between modelled dust emission flux F (PM10), saltation flux Q, and ratio F/Q with friction velocity u_* for $c_y = 6 \times 10^{-5}$ and optimized parameters κ and P. Vertical gray lines indicate the standard deviation.

optimized to obtain best estimates for six dust events observed on a crusted site with sandy soil texture during spring 2016. Observations showed that the rate of dust emission as a function of friction velocity was not constant, but changed between the events, suggesting that the soil surface conditions varied. The parameter estimates obtained through our numerical experiments not only confirmed this variation, but also supported interpretation of the variability. By adapting aggregate stability and soil plastic pressure (both are scheme parameters), most of the observed variability in dust emission efficiency could be explained. While no direct field measurements of these parameters were possible in our study, the estimated parameters agree with values obtained in previous studies (e.g. Zimbone et al., 1996; Rice et al., 1997; Goossens, 2004). However, a comparison with direct measurements of P and κ is desirable for the future as an independent reference.

The correct estimation of saltation flux as an input to the dust emission scheme is critical to determine dust emission at a location. Q is normally parameterised as a uniform equilibrium process, which poses problems for situations in which saltation is supply-limited such as on crusted surfaces. Here, we used a heuristic approach to estimate Q combining the numerical equilibrium-Q estimate with a scaling factor obtained from observations. This approximation was sufficient for our test site on which the amount of sand particles for saltation was large, because friction velocity was still the main determining factor for saltation flux. On sites with only a small amount of sand particles, large friction velocity is still a necessary, but not a sufficient condition for saltation to occur. Under these circumstances, a physics-based parameterisation of non-equilibrium saltation flux (e.g. Selmani et al., 2017) is necessary. Such a parameterisation needs information about particle-availability, similar to that obtained here from field measurements. It is, however, impossible to collect such detailed surface data like the one use here in the field on a continental or even global scale. It is therefore necessary to advance on the use of new high-resolution satellite data to determine, e.g. crusted surface areas. The better specification of soil-surface conditions will substantially improve dust emission estimates and help to constrain global dust aerosol along with its climate impacts.

Appendix A: Land-surface monitoring

Land-surface cover was monitored for each event using the line-point-intercept (LPI) method (Herrick et al., 2005) in which any cover is recorded that touches a vertical pin. Readings were done every 25 cm along three parallel 50 m long lines, 20 m apart (see also Fig. 3). The average results for each site are shown in Fig. A1. According to the LPI results, the surface conditions changed only slightly at a site between different events (Fig. A1 for Site C) except for Site D where substantially more crust cover was recorded for a measurement episode in January compared to May (26% compared to 5%, not shown) due to residual soil moisture from antecedent rainfall. It is important to note that the LPI method as applied here required "loose erodible material" (LEM) (Klose et al., 2017) to be recorded as surface condition if loose particles, e.g. sand grains, can be seen at a surface, even if only few particles rested on top of a surface crust. This is particularly relevant for Site C on which a subjective estimate of crust cover would have resulted in a much larger percentage than $\sim$8% on average as it was obtained using LPI. Site C also showed visible changes in surface conditions, i.e. eroded surface crust, which were not evident from the LPI results.

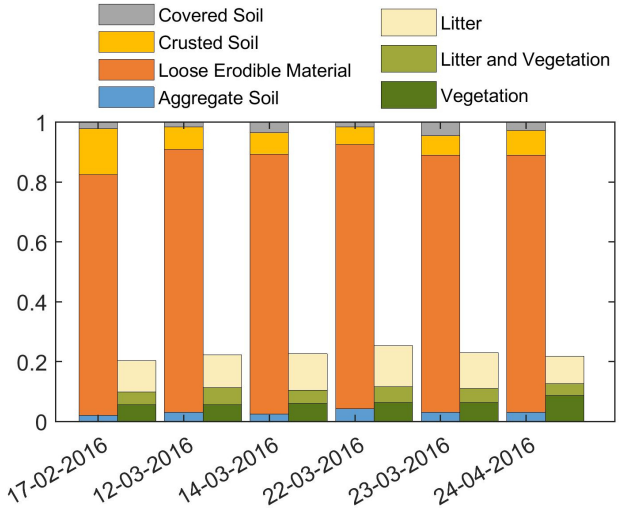

Figure A1. (top) Average cover fractions at the surface (aggregated soil, loose erodible material, crusted soil, and covered soil [plant bases and gravel]) and in the canopy layer (organic litter, litter and vegetation, vegetation only) for the different monitoring dates on Site C obtained using the line-point-intercept method.

Appendix B: Estimation of quantities describing the atmospheric state and sediment transport

At Sites A-D, wind speed measurements were conducted at four heights (0.7, 1.4, 2.4, and 4.8 m; wind direction at 4.8 m height) and temperature measurements at two heights (2 m and 5 m). The sites were further equipped with a rain gauge and radiometer. Sites E and F were installed temporarily and their setup slightly differed from Sites A-D in terms of measurement heights. Rain gauge and radiometer were not available on Sites E and F. Data was recorded at intervals of 1 min before 28 Mar 2016 and of 1 s afterwards.

Friction velocity, u_* [$\mathrm{m\,s^{-1}}$], was iteratively calculated based on the vertical profile of 15-min running averages of measured wind speeds based on Benoit (1977) as

$$\frac{u(z)}{u_*} = \frac{1}{k}\left\{\ln\left(\frac{z}{z_0}\right) + \ln\left[\frac{\left(\zeta_0^2+1\right)\left(\zeta_0+1\right)^2}{\left(\zeta^2+1\right)\left(\zeta+1\right)^2}\right] + 2\left[\tan^{-1}\left(\zeta\right) - \tan^{-1}\left(\zeta_0\right)\right]\right\}, \tag{B1}$$

where $\zeta = (1-15z/L)$, $\zeta_0 = (1-15z_0/L)$ and $L = \left(-u_*^3\theta\right)/\left(kg\overline{w'\theta'}_0\right)$ is the Obukhov-length. Herein z is height, z_0 the aerodynamic roughness length, k the von-Kárman constant, θ a reference potential temperature, g gravitational acceleration, and $\overline{w'\theta'}_0$ the surface kinematic heat flux. For neutral conditions ($z/L \to 0$), Eq. (B1) becomes $\frac{u(z)}{u_*} = \frac{1}{k}\ln\left(z/z_0\right)$. The heat flux, $H = \rho c_p \overline{w'\theta'}_0$, was in turn obtained as

$$H = \rho c_p \frac{T_0 - T_r}{r_a} \tag{B2}$$

where T_0 is ground temperature, T_r the temperature at reference heigth z_r, and $r_a = \left(C_h u_r\right)^{-1}$ the bulk aerodynamic resistance between z_0 and z_r with bulk heat transfer coefficient C_h (e.g. Shao, 2008). T_0 was obtained from radiometer measurements

Table B1. List of equations used to iteratively estimate u_* and w_*.

Quantity [Unit]	Symbol	Equation	Reference
Friction velocity [$\mathrm{m\,s^{-1}}$]	u_*	Eq. (B1)	Benoit (1977)
Obukhov length [m]	L	$L = \left(-u_*^3\theta\right) / \left(kg\overline{w'\theta'}_0\right)$	Stull (1988)
Heat flux [$\mathrm{W\,m^{-2}}$]	H	Eq. (B2)	Stull (1988)
Bulk aerodynamic resistance [$\mathrm{s\,m^{-1}}$]	r_a	$r_a = \left(C_h u_r\right)^{-1}$	Shao (2008)
Heat transfer coefficient [1]	C_h	$C_h = \frac{k}{\psi_m \psi_h}$	Shao (2008)
Non-dimensional function of ζ in wind profile	ψ_m	$\psi_m = \begin{cases} \ln\left(\frac{z}{z_0}\right) + 4.7\zeta & \text{for } \zeta > 0 \\ \ln\left(\frac{z}{z_0}\right) - \Psi_1 & \text{for } \zeta \leq 0 \end{cases}$	Benoit (1977); Shao (2008)
		$\Psi_1 = \ln\left[\frac{\left(\phi_m\left(\zeta_0\right)^2 + 1\right)\left(\phi_m\left(\zeta_0\right) + 1\right)^2}{\left(\phi_m\left(\zeta\right)^2 + 1\right)\left(\phi_m\left(\zeta\right) + 1\right)^2}\right] + 2\left[\tan^{-1}\left(\phi_m\left(\zeta\right)\right) - \tan^{-1}\left(\phi_m\left(\zeta_0\right)\right)\right]$	
		$\phi_m = \begin{cases} 1 + 4.7\zeta & \text{for } \zeta > 0 \\ \left(1 - 15\zeta\right)^{-1/4} & \text{for } \zeta \leq 0 \end{cases}$	
Non-dimensional function of ζ in temperature profile	ψ_h	$\psi_h = \begin{cases} 0.74\ln\left(\frac{z}{z_0}\right) + 4.7\zeta & \text{for } \zeta > 0 \\ 0.74\left[\ln\left(\frac{z}{z_0}\right) - \Psi_2\right] & \text{for } \zeta \leq 0 \end{cases}$	Benoit (1977); Shao (2008)
		$\Psi_2 = \ln\left(\left[1 + 0.74\phi_h^{-1}\right]/2\right)$	
		$\phi_h = \begin{cases} 0.74 + 4.7\zeta & \text{for } \zeta > 0 \\ \left(1 - 9\zeta\right)^{-1/2} & \text{for } \zeta \leq 0 \end{cases}$	
Convective scaling velocity [$\mathrm{m\,s^{-1}}$]	w_*	$w_* = \left(\frac{g}{\theta}\overline{w'\theta'_0} z_i\right)^{1/3}$	Stull (1988)

of surface longwave radiative flux where available. To determine the convective scaling velocity, w_* [$\mathrm{m\,s^{-1}}$] (see Tab. B1), potential temperature, θ, was computed from 2 m temperature, $T_{2\mathrm{m}}$, and planetary boundary layer height, z_i, was taken from the National Centers for Environmental Prediction (NCEP) Global Data Assimilation System (GDAS) Final Analysis (National Centers for Environmental Prediction, National Weather Service, NOAA, U.S. Department of Commerce, 2015).

The total streamwise saltation flux, Q [$\mathrm{\mu g\,m^{-1}\,s^{-1}}$], is defined as the vertical integral of the height-dependent streamwise saltation flux, $q\left(z\right)$,

$$Q = \int_0^\infty q\left(z\right) dz. \tag{B3}$$

Q obtained from the MWAC samples can be interpreted as an average over the time of active sediment transport during sampling. In that case, $q_{\mathrm{MWAC}}(z) = m_z/(A_q t_q)$ with m_z being the sample mass collected at height z and A_q and t_q being the MWAC inlet cross-sectional area ($0.47\,\mathrm{cm}^2$) and duration of active sediment transport, respectively. Here, t_q was determined as the duration for which friction velocity, u_*, exceeded the threshold for sediment entrainment, u_{*t}, during the time of MWAC exposure. Threshold friction velocity, u_{*t}, was estimated as the minimum value per event obtained with the time fraction equivalence method (Barchyn and Hugenholtz, 2011) for 1 min intervals in the case of 1 s data (the Gaussian time fraction equivalence method in the case of 1 min data) using the Wenglor saltation counts as input. Wenglor saltation counts were not used directly to determine t_q, because particle movement depends on particle availability and might vary within the site. Approximating the vertical profile of q as

$$q(z) = q_c \exp(-\beta z), \tag{B4}$$

Q was obtained analytically through vertical integration of $q(z)$ with q_c and β obtained through nonlinear regression. Profiles for which the coefficient of determination, R^2, was below 0.5 were excluded. For the events on Site C, R^2 was greater than 0.99 in all cases. The final Q per event was obtained as average between the five profiles obtained for each of the MWAC masts.

For the SANTRI records, it is $q_{\mathrm{SANTRI}}(z) = \frac{1}{A_s}\sum_{\mathrm{bins}} \rho_p \frac{\pi d_{\mathrm{bin}}^3}{6} N_{\mathrm{bin}}$, where A_s is the laser sensing area ($A_s = 1.27 \times 9.53\,\mathrm{mm}^2$), N_{bin} are the counts per bin registered by the instrument, and ρ_p is particle density, here assumed as $2650\,\mathrm{kg\,m^{-3}}$. d_{bin} is the logarithmic average diameter per bin. The lower and upper diameter limits for each bin vary with time and were obtained based on the recorded sensor reference voltage level. Note that the lowest of the seven bins was excluded due to a relatively large noise-level and the largest bin was excluded, because it does not have an upper diameter limit. Using $q_{\mathrm{SANTRI}}(z)$ for the two sensing heights, Eq. (B4) was solved analytically using 1-min integrals. Q was again computed through integration of Eq. (B4) and averaged over the four sensor pair combinations and two instruments.

The dust emission flux, F [$\mu\mathrm{g\,m^{-2}\,s^{-1}}$], was calculated based on 15-min running averages of measured dust concentration at two heights as described by Shao (2008, Chapter 7). A stability correction, comparable to that used to estimate u_*, and a correction for particle settling were applied as suggested by Shao (2008). Dust concentration measurements used for the flux calculations underwent individual quality control and inter-calibration for each measurement episode and instrument records that showed any unreasonable trend or offset compared to the other instruments and events were excluded from further analyses. Quality control and inter-calibration was conducted using the following procedure:

1. The inter-instrument offset was estimated using short-duration ($\sim 10\,\mathrm{min}$) measurements conducted under laboratory conditions before each field measurement episode after zero-calibration of the instruments. Despite zero-calibration, the instruments showed a small offset, which was computed as deviation of the robust mean concentration (average obtained excluding the largest and smallest 42.5% of the values, i.e. using only the 25% central values) of each instrument from its average.

2. A linear regression was conducted on the concentrations recorded during the field measurements with the previous correction applied. Herein the same temporal data points were used for all instruments to ensure consistent conditions.

The slopes obtained from the linear model were compared to detect if any instrument showed unrealistic trends, i.e. slope values identified as outliers. A value is considered to be an outlier if it deviates more than three median absolute deviations (MAD) from the median (Hampel, 1974; Leys et al., 2013). So identified instruments – if any – would be excluded from further analysis for the episode under consideration.

3. The first 2 hrs of field measurements, during which dust concentrations were generally low and close to a background value, were used to compute an inter-instrument offset similar to the laboratory-offset described before. The field-offset was computed considering only instruments mounted at the same height to account for variations of aerosol concentration with height already at background levels. The total offset-correction was obtained as sum of the laboratory and field offset.

For one of the three co-located instrument pairs, both instruments showed substantially different readings compared to one another and the other instruments. This pair was therefore excluded from further analysis and from inter-calibration for all episodes.

Acknowledgements. This study was funded by the German Research Foundation (Deutsche Forschungsgemeinschaft, DFG) grant KL 2932/1-1 awarded as a postdoctoral research fellowship to MK. TEG and RSVP acknowledge support from NASA grant NNX16AH13G. NPW acknowledges support through funding from the Department of Interior, Bureau of Land Management. We thank Ralph Lorenz for providing pressure loggers and the Davis anemometer used on Site F. We also thank Sharalyn Peterson, Justin Van Zee, and Bradley Cooper for field and lab assistance. LPI point data were recorded using DIMA (https://jornada.nmsu.edu/monit-assess/dima). Any use of trade, product, or firm names is for descriptive purposes only and does not imply endorsement by the U.S. Government. The USDA is an equal opportunity provider and employer. We thank two anonymous reviewers for their positive and helpful comments.

References

Baddock, M. C., Zobeck, T. M., Van Pelt, R. S., and Fredrickson, E. L.: Dust emissions from undisturbed and disturbed, crusted playa surfaces: Cattle trampling effects, Aeolian Res., 3, 31–41, https://doi.org/10.1016/j.aeolia.2011.03.007, 2011.

Barchyn, T. E. and Hugenholtz, C. H.: Comparison of four methods to calculate aeolian sediment transport threshold from field data: Implications for transport prediction and discussion of method evaluation, Geomorphology, 129, 190–203, https://doi.org/10.1016/j.geomorph.2011.01.022, 2011.

Benoit, R.: On the integral of the surface layer profile-gradient functions, J. Appl. Meteor., 16, 859–860, https://doi.org/10.1175/1520-0450(1977)016<0859:OTIOTS>2.0.CO;2, 1977.

Darmenova, K., Sokolik, I. N., Shao, Y., Marticorena, B., and Bergametti, G.: Development of a physically based dust emission module within the Weather Research and Forecasting (WRF) model: Assessment of dust emission parameterizations and input parameters for source regions in Central and East Asia, J. Geophys. Res., 114, D14201, https://doi.org/10.1029/2008JD011236, 2009.

Etyemezian, V., Nikolich, G., Nickling, W., King, J. S., and Gillies, J. A.: Analysis of an optical gate device for measuring aeolian sand movement, Aeolian Res., 24, 65–79, https://doi.org/10.1016/j.aeolia.2016.11.005, 2017.

Fryrear, D. W., Saleh, A., Bilbro, J. D., Schomberg, H. M., Stout, J. E., and Zobeck, T. M.: Revised Wind Erosion Equation (RWEQ), Technical Bulletin No. 1, Wind Erosion and Water Conservation Research Unit, USDA-ARS, Southern Plains Area Cropping Systems Research Laboratory, 1998.

Gillette, D. A., Blifford Jr., I. H., and Fenster, C. R.: Measurements of aerosol size distributions and vertical fluxes of aerosols on land subject to wind erosion, J. Appl. Meteor., pp. 977–987, 1972.

Gillette, D. A., Adams, J., Muhs, D., and Kihl, R.: Threshold friction velocities and rupture moduli for crusted desert soils for the input of soil particles into the air, J. Geophys. Res., 87, 9003–9015, https://doi.org/10.1029/JC087iC11p09003, 1982.

Gomes, L., Bergametti, G., Dulac, F., and Ezat, U.: Assessing the actual size distribution of atmospheric aerosols collected with a cascade impactor, J. Atmos. Sci., 21, 47–59, 1990.

Goossens, D.: Effect of crusting on the emission and transport of wind-eroded sediment: field measurements on loamy sandy soil, Geomorphology, 58, 147–160, https://doi.org/10.1016/S0169-555X(03)00229-0, 2004.

Goossens, D., Nolet, C., Etyemezian, V., Duarte-Campos, L., Bakker, G., and Riksen, M.: Field testing, comparison, and discussion of five aeolian sand transport measuring devices operating on different measuring principles, Aeolian Res., 32, 1–13, https://doi.org/10.1016/j.aeolia.2018.01.001, 2018.

Hagen, L. J., Skidmore, E. L., and Saleh, A.: Wind erosion: Prediction of aggregate abrasion coefficients, Trans. ASAE, 35, 1847–1850, 1992.

Hampel, F. R.: The influence curve and its role in robust estimation, J. Am. Stat. Assoc., 69, 383–393, 1974.

Herrick, J. E., Zee, J. W. V., Havstad, K. M., Burkett, L. M., and Whitford, W. G.: Monitoring manual for grassland, shrubland and savanna ecosystems, I, http://www.fwspubs.org/doi/suppl/10.3996/052014-JFWM-039/suppl_file/052014-jfwm-039r1-s04.pdf?code=ufws-site, distributed by: The University of Arizona Press, Tucson, Arizona, USA, 2005.

Houser, C. A. and Nickling, W. G.: The emission and vertical flux of particulate matter $< 10\mu$m from a disturbed clay-crusted surface, Sedimentology, 48, 255–267, https://doi.org/10.1046/j.1365-3091.2001.00359.x, 2001a.

Houser, C. A. and Nickling, W. G.: The factors influencing the abrasion efficiency of saltating grains on a clay-crusted playa, Earth Surf. Proc. Landforms, 26, 491–505, https://doi.org/10.1002/esp.193, 2001b.

Hugenholtz, C. H. and Barchyn, T. E.: Laboratory and field performance of a laser particle counter for measuring aeolian sand transport, J. Geophys. Res., 116, F01010, https://doi.org/10.1029/2010JF001822, 2011.

Kawamura, R.: Study of sand movement by wind, in: In: Hydraulic Eng. Lab. Tech. Rep., pp. 99–108, University of California, Berkeley, CA, HEL-2-8, 1964.

Klose, M., Gill, T. E., Webb, N. P., and Zee, J. W. V.: Field sampling of loose erodible material: A new method to sample the full particle-size spectrum, Aeolian Res., 28, 83–90, https://doi.org/10.1016/j.aeolia.2017.08.003, 2017.

Kuntze, H., Schäfer, W., and Frielinghaus, M.: Quantifizierung der Bodenerosion durch Wind, Final report of the bmbf-project, Federal Agency of Soil Research of Lower Saxony, Bremen, Germany, 1990.

Leys, C., Ley, C., Klein, O., Bernard, P., and Licata, L.: Detecting outliers: Do not use standard deviation around the mean, use absolute deviation around the median, J. Exp. Psychol., 49, 764–766, 2013.

Macpherson, T., Nickling, W. G., Gillies, J. A., and Etyemezian, V.: Dust emissions from undisturbed and disturbed supply-limited desert surfaces, Journal of Geophysical Research: Earth Surface, 113, F02S04, https://doi.org/10.1029/2007JF000800, 2008.

McKenna Neuman, C., Maxwell, C. D., and Wayne Boulton, J.: Wind transport of sand surfaces crusted with photoautotrophic microorganisms, Catena, 27, 229–247, https://doi.org/10.1016/0341-8162(96)00023-9, 1996.

Middleton, N. J.: Desert dust hazards: A global review, Aeolian Res., 24, 53–63, https://doi.org/10.1016/j.aeolia.2016.12.001, 2017.

National Centers for Environmental Prediction, National Weather Service, NOAA, U.S. Department of Commerce: NCEP GDAS/FNL 0.25 Degree Global Tropospheric Analyses and Forecast Grids, https://doi.org/10.5065/D65Q4T4Z, 2015.

Raupach, M. R. and Lu, H.: Representation of land-surface processes in aeolian transport models, Environmental Modelling & Software, 19, 93 – 112, https://doi.org/10.1016/S1364-8152(03)00113-0, modelling of Wind Erosion and Aeolian Processes, 2004.

Raupach, M. R., Gilette, D. A., and Leys, J. F.: The effect of roughness elements on wind erosion threshold, J. Geophys. Res., 98, 3023–3029, https://doi.org/10.1029/92JD01922, 1993.

Rice, M. A. and McEwan, I. K.: Crust strength: A wind tunnel study of the effect of impact by saltating particles on cohesive soil surfaces, Earth Surf. Proc. Landforms, 26, 721–733, https://doi.org/10.1002/esp.217, 2001.

Rice, M. A., Mullins, C. E., and McEwan, I. K.: An analysis of soil crust strength in relation to potential abrasion by saltating particles, Earth Surf. Proc. Landforms, 22, 869–883, https://doi.org/10.1002/(SICI)1096-9837(199709)22:9<869::AID-ESP785>3.0.CO;2-P, 1997.

Selmani, H., Valance, A., Ould El Moctar, A., Dupont, P., and Zegadi, R.: Aeolian sand transport in out-of-equilibrium regimes, Geophys. Res. Lett., 45, 1838–1844, https://doi.org/10.1002/2017GL076937, 2017.

Shao, Y.: A model for mineral dust emission, J. Geophys. Res., 106, 20 239–20 254, 2001.

Shao, Y.: Simplification of a dust emission scheme and comparison with data, J. Geophys. Res., 109, D10202, https://doi.org/10.1029/2003JD004372, 2004.

Shao, Y.: Physics and Modelling of Wind Erosion, Springer–Verlag, Berlin, 2 edn., 2008.

Shao, Y. and Lu, H.: A simple expression for wind erosion threshold friction velocity, J. Geophys. Res., 105, 22 437–22 443, 2000.

Shao, Y., Raupach, M. R., and Leys, J. F.: A model for predicting aeolian sand drift and dust entrainment on scales from paddock to region, Aust. J. Soil Res., 34, 309–342, 1996.

Shao, Y., Ishizuka, M., Mikami, M., and Leys, J. F.: Parameterization of size-resolved dust emission and validation with measurements, J. Geophys. Res., 116, https://doi.org/10.1029/2010JD014527, 2011.

Shao, Y., Nickling, W., Bergametti, G., Butler, H., Chappell, A., Findlater, P., Gillies, J., Ishizuka, M., Klose, M., Kok, J. F., Leys, J., Lu, H., Marticorena, B., McTainsh, G., McKenna-Neuman, C., Okin, G. S., Strong, C., and Webb, N.: A tribute to M. R. Raupach for contributions to aeolian fluid dynamics, Aeolian Res., 19, 37–54, https://doi.org/10.1016/j.aeolia.2015.09.004, 2015.

Sperazza, M., Moore, J., and Hendrix, M.: High-resolution particle size analysis of naturally occurring very fine-grained sediment through laser diffractometry, J. Sed. Res., 74, 736–743, 2004.

Stull, R. B.: An Introduction to Boundary Layer Meteorology, Kluwer Academic Publishers, Norwell, 1988.

Webb, N. P., Galloza, M. S., Zobeck, T. M., and Herrick, J. E.: Threshold wind velocity dynamics as a driver of aeolian sediment mass flux, Aeolian Res., 20, 45–58, https://doi.org/10.1016/j.aeolia.2015.11.006, 2016.

Wilson, S. J. and Cooke, R. U.: Wind erosion, in: Soil erosion, edited by Kirkby, M. J. and Morgan, R. P. C., pp. 217 – 251, Wiley, Chichester, 1980.

Zimbone, S. M., Vickers, A., Morgan, R. P. C., and Vella, P.: Field investigations of different techniques for measuring surface soil shear strength, Soil Technology, 9, 101–111, https://doi.org/10.1016/0933-3630(96)00002-5, 1996.

Zobeck, T. M.: Abrasion of crusted soils: Influence of abrader flux and soil properties, Soil Sci. Soc. Am. J., 55, 1091–1097, https://doi.org/10.2136/sssaj1991.03615995005500040033x, 1991.

Zobeck, T. M.: Rapid soil particle size analyses using laser diffraction, Appl. Eng. Agric., 20, 633–639, 2004.